

A Study on the Largest Hydraulic-Fracturing-Induced Earthquake in Canada: Observations and Static Stress-Drop Estimation

Bei Wang^{*1,2}, Rebecca M. Harrington³, Yajing Liu⁴, Honn Kao^{1,2}, and Hongyu Yu²

ABSTRACT

On 17 August 2015, an M_w 4.6 earthquake occurred northwest of Fort St. John, British Columbia, possibly induced by hydraulic fracturing (HF). We use data from eight broadband seismometers located ~ 50 km from the hypocenter to detect and estimate source parameters of more than 300 events proximal to the mainshock. Stress-drop values estimated using seismic moment and corner frequency from single-event spectra and spectral ratios range from ~ 1 to 35 MPa, within the typical range of tectonic earthquakes. We observe an ~ 5 -day delay between the onset of fluid injection and the mainshock, a b -value of 0.78 for the sequence, and a maximum earthquake magnitude larger than the prediction based on the total injection volume, suggesting that the M_w 4.6 sequence occurred on a pre-existing fault and that the maximum magnitude is likely controlled by tectonic conditions. Results presented here show that pre-existing fault structures should be taken into consideration to better estimate seismic hazard associated with HF operations and to develop schemes for risk mitigation in close proximity to HF wells.

KEY POINTS

- We study the largest hydraulic-fracturing (HF) earthquake in Canada, and infer it was on a pre-existing fault.
- M_{\max} of HF-induced earthquakes are site-dependent, with stress-drop values similar to tectonic events.
- Proximity of HF wells to pre-existing fault structures should be considered in seismic hazard estimation.

Supplemental Material

INTRODUCTION

Induced seismicity refers to earthquakes caused by stress perturbations imposed by anthropogenic activities. Recent studies have shown a strong positive correlation between earthquakes and fluid injection related to wastewater disposal and hydraulic fracturing (HF). In particular, a number of large (M 4+) HF-induced earthquakes have occurred in North America and in China (e.g., [B.C. Oil and Gas Commission, 2012](#); [Ellsworth, 2013](#); [Weingarten *et al.*, 2015](#); [Atkinson *et al.*, 2016](#); [Lei *et al.*, 2019](#)). For instance, in the central United States (CUS), induced earthquakes are caused presumably by pore-pressure and elastic stress changes that destabilize pre-existing faults within confined subsurface zones due to saltwater disposal (e.g., [Ellsworth, 2013](#); [Keranen *et al.*, 2014](#); [Weingarten *et al.*, 2015](#)), whereas in western Canada, HF has been inferred as the main contributor to the drastic increase in seismicity since

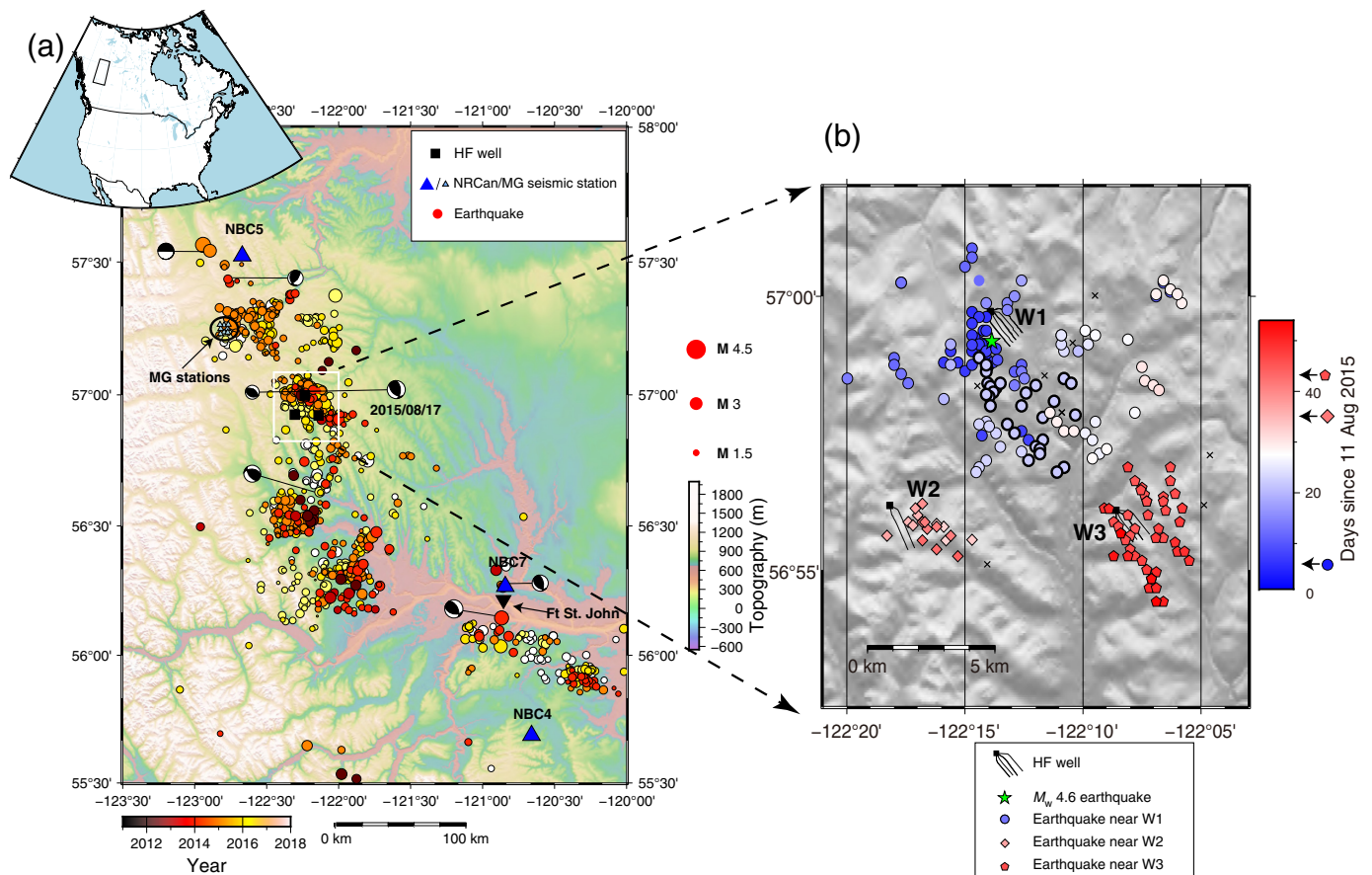
~ 2008 ([Atkinson *et al.*, 2016](#)). Recent studies in the Sichuan basin, China, also suggest a close correlation between induced seismicity and HF operations in which some of the largest potential HF-induced earthquakes have reached an M_w of 5.7 ([Lei *et al.*, 2019](#)). In addition, an HF-induced M_w 4.7 earthquake on 28 January 2017 most likely occurred in the pre-Triassic sedimentary layer, rather than in the crystalline basement ([Lei *et al.*, 2017](#)), suggesting that HF injection fluids may interact with faults at a variety of depths. Both poroelastic stress transfer and pore-pressure diffusion may act as triggering mechanisms of induced earthquakes. Specifically, static stress transmitted through the rock matrix could introduce near-instantaneous stress perturbations at distances of up to ~ 4 km from the injection point (e.g., [Deng *et al.*, 2016](#); [Yu *et al.*, 2019](#)), whereas fluid pressure diffusion may act on short time scales within ~ 1 km of the well bore and with a delayed response at farther distances (e.g., [Atkinson *et al.*, 2016](#); [Bao and](#)

1. Now at School of Earth and Ocean Sciences, University of Victoria, Victoria, British Columbia, Canada; 2. Pacific Geoscience Centre, Geological Survey of Canada, Sidney, British Columbia, Canada; 3. Ruhr University Bochum, Institute of Geology, Mineralogy, and Geophysics, Bochum, Germany; 4. Department of Earth and Planetary Sciences, McGill University, Montreal, Quebec, Canada

*Corresponding author: bei.wang@mail.mcgill.ca

Cite this article as Wang, B., R. M. Harrington, Y. Liu, H. Kao, and H. Yu (2020). A Study on the Largest Hydraulic-Fracturing-Induced Earthquake in Canada: Observations and Static Stress-Drop Estimation, *Bull. Seismol. Soc. Am.* **XX**, 1–12, doi: [10.1785/0120190261](https://doi.org/10.1785/0120190261)

© Seismological Society of America



Eaton, 2016; Mahani *et al.*, 2017; Schultz *et al.*, 2018; Yu *et al.*, 2019).

In the past decade, British Columbia (BC) has become one of the most active regions for the exploitation of unconventional hydrocarbon resources in the western Canada sedimentary basin (WCSB). The Montney Formation in the WCSB is one of the primary focuses of gas reservoirs in the northeastern BC due to the large amount of shale gas and tight gas reserves. The Montney Formation is located near the Fort St. John (FSJ) area and is mainly composed of turbidite siltstone and dark gray shale (Moslow, 2000). An increase in industrial injection activity starting in 2011 has been commensurate with the increase of local seismicity (e.g., B.C. Oil and Gas Commission, 2012). For instance, 10 $M > 3$ earthquakes were reported by Natural Resources Canada (NRCAN) in northeastern BC between 2003 and 2010, compared with 58 $M > 3$ events between 2011 and 2019 (Fig. 1a), including the 2015 M_w 4.6 FSJ earthquake and the 2018 M_w 4.5 earthquake near Dawson Creek. The frequency with which $M > 4$ earthquakes occur in the WCSB has raised many questions, such as, what is the spatiotemporal correlation between injection activity and induced earthquakes? What are the source parameters of induced earthquakes and what implications do the scaling of source parameters have on the implied triggering mechanisms?

Figure 1. (a) Seismicity and station distribution in northeastern British Columbia, 2011–2018. Earthquake symbol size corresponds to magnitude, and color corresponds to origin time. Natural Resources Canada (NRCAN) stations in operation since 2011 shown in large triangles; MG stations operating from 13 May to 13 October 2015 shown in small triangles. Black squares show the locations of active hydraulic-fracturing (HF) wells during August–October 2015. Focal mechanism solutions are from the NRCAN database. (b) Relative relocations of 191 earthquakes detected using multistation matched-filter (MMF) detection. Horizontal well injection data is from the BC Oil and Gas Commission database. The star indicates the location of the M_w 4.6 mainshock. Symbol shapes differentiate clusters associated with respective HF wells, W1, W2, and W3. Circles with thicker outlines denote earthquakes that occurred on 2 September 2015. Crosses denote the location of the eight templates used in the enhanced MMF detection. The inset in (a) marks the study area. The color version of this figure is available only in the electronic edition.

On 17 August 2015, the largest potentially HF-induced earthquake in the WCSB occurred near FSJ, northeastern BC, with a reported M_w 4.6. The earthquake was located within 1 km of an active HF well (W1, Fig. 1). A total volume of $\sim 65,000$ m³ was injected at the depth of ~ 1.9 km into the Lower Montney Formation in the five days prior to the earthquake. Here, we examine in detail the seismicity distribution surrounding the M_w 4.6 mainshock through enhanced earthquake detection and double-difference earthquake relocation, as well as earthquake spectral analysis. The primary objectives

of this study are (1) to establish and quantify correlations between the M_w 4.6 sequence and injection history of nearby wells and (2) to estimate event source parameters (seismic moment, corner frequency, and static stress drop) to quantify the magnitude and scaling of stress-drop values with event size. In the following, we will show a spatial–temporal correlation between the seismicity and proximity to HF wells and examine a possible correlation of event size with injection volume. We will also show evidence that the stress-drop values for the induced earthquake sequence fall within the range typically observed for tectonic events.

DATA ACQUISITION

We use data from a temporary deployment of eight broadband seismic stations (MG01–MG08 of the QM network, 200 Hz sampling rate) northwest of FSJ, supplemented by three NRCAN regional stations (NBC4, NBC5, and NBC7 of the CN network, 100 Hz sampling rate) to study the M_w 4.6 sequence (located at ~50 km southeast of the MG seismic stations, Fig. 1a). The MG stations recorded data from 13 May to 13 October 2015, but we focus on seismicity between 11 August and 7 October 2015 as prior and subsequent seismic activity in the study area was negligible. Four of the MG stations had unlocked Global Positioning System signals during part of the deployment period, which caused a nonnegligible timing error. We applied an ambient noise correction to reduce the timing error from ~1 to ~0.1 s (details of the timing correction can be found in the supplemental material to this article and in Yu *et al.*, 2019).

ENHANCED CATALOG AND EVENT LOCATION

We first use the multistation matched-filter (MMF) approach with NRCAN-reported earthquakes as templates to enhance the completeness of our catalog for the time period indicated previously using MG and NRCAN stations as shown in Figure 1. We then calculate the initial hypocentral locations of the MMF detections through both grid-search and double-difference relocation. Finally, we estimate the source parameter of each event. The following two sections detail the methods used to build the MMF catalog with relative relocations and the timing of earthquake occurrence with injection activity.

Enhanced catalog building using MMF detection

The NRCAN catalog contains 25 events during the time window of this study (August 11 to 7 October 2015), ranging in magnitude from 1.4 to 4.6. To maximize the number of locatable earthquakes, we perform an enhanced detection using an MMF approach. The MMF approach searches for signals in the continuous waveforms by cross-correlating template waveforms across multiple stations and summing the cross-correlation coefficients (e.g., Skoumal *et al.*, 2015). When the summed correlation coefficients exceed some predetermined threshold, a detection is declared. We follow the methods of Wang *et al.*

(2015, 2018) and use continuous waveforms from the eight MG stations and three NRCAN stations with the eight template earthquakes that occurred following the M_w 4.6 earthquake (M_w 1.4–4.6; all of the other cataloged events have been detected by our MMF method). The eight templates were chosen by grouping the original 25 cataloged events based on waveform similarity and using the largest amplitude event in each group (to reduce the number of potential templates and thereby the computation time of the MMF detection).

Prior to performing the cross correlation, we remove the instrument response and apply a band-pass filter of 5–15 Hz, which is the frequency band of the dominant energy of seismicity in this study, to both the templates and the continuous waveforms. We then calculate the cross-correlation values at each station in timesteps of 0.01 s. We allow for time-window shifts of up to 2 s between stations to maximize the cross-correlation values before summing, thus increasing the chance of detecting earthquakes offset from the template locations (i.e., noncollocated events). A detection is declared when the cross-correlation value exceeds 18 times the mean absolute deviation (MAD) value corresponding to the 75th percentile for a symmetric distribution with zero mean. The empirically set MAD value allows for the added advantage of detecting a larger number of candidate events, from which the false detections are removed by manual inspection. We also visually inspect all detections to remove events with less than five phase picks that cannot subsequently be located. The previous procedure results in a total of 468 automatic detections, of which 323 are selected for location.

Location and temporal correlation with injection

We manually pick *P*- and *S*-wave arrival times for the 323 detections outlined previously and calculate their initial hypocentral locations using the CRUST 1.0 velocity model with a $1^\circ \times 1^\circ$ box centered at (57.5° N, 122.5° W) (Laske *et al.*, 2013; Fig. S1). Phase picks are primarily from MG stations, with some phase picks from NBC4, NBC5, and NBC7 for the larger events for which it is possible to constrain phase arrivals using cross-correlation time lags (Fig. S2). The hypocenter estimation uses a two-step approach, beginning with an initial coarse matrix grid search followed by location and origin-time refinement with a nonlinear iterative method. The details of the two-step grid-search method are explained in supplemental material and Figure S3.

Next, we employ the double-difference relocation method (hypoDD) to further refine the earthquake locations (Waldhauser and Ellsworth, 2000). We use phase picks and differential travel times determined with cross correlation of waveforms as the hypoDD input, and the parameter settings are listed in Table S1. The final relocation result retains 191 of the initial 323 events. We calculate the spatial uncertainties of relocated hypocenters using 1000 bootstrap random replacement trials, taking samples from observed residual distribution

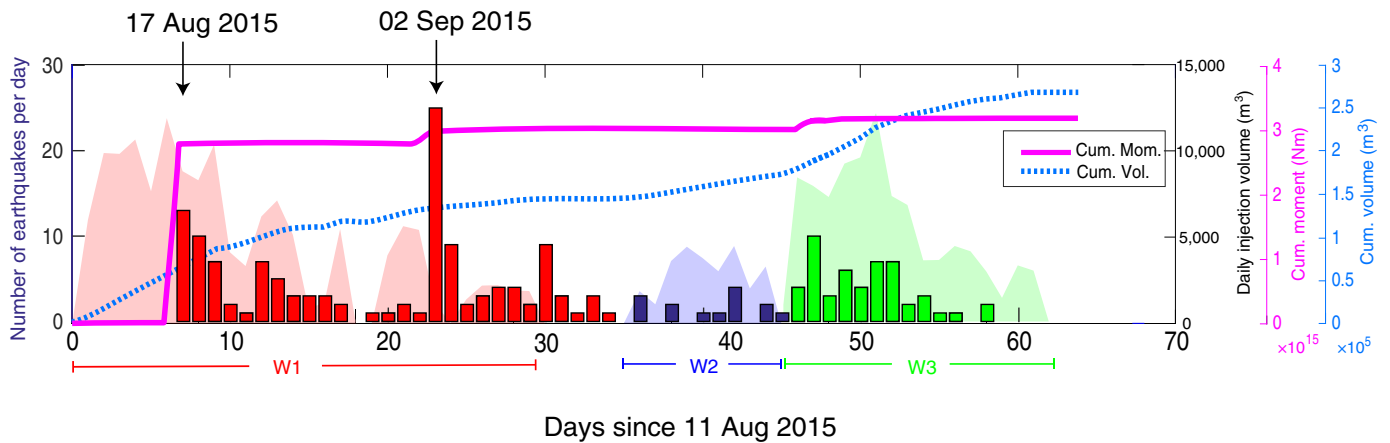


Figure 2. Daily seismicity (colored bars) and daily injection volume (colored shaded areas) since 11 August 2015, one day before the start of HF injection at W1. The active injection periods for each well are indicated along the horizontal axis. Solid line indicates the cumulative moment for the MMF-detected earthquakes shown in the histogram; dashed line denotes the cumulative injection volume from the three HF wells. The color version of this figure is available only in the electronic edition.

to replace the final residuals, following the method of Harrington *et al.* (2015) and Yu *et al.* (2016) (Table S2). We only retain events with horizontal and vertical errors of less than 3 km. We note that source depths may not be well constrained due to the large source–station distances and that the horizontal relative locations perpendicular to the back azimuth of available MG and NRCan stations may be not as well constrained as the direction parallel to the back azimuth. Figure 1b shows the 191 relocated events, and their spatial distribution suggests three earthquake sequences that correlate spatially with nearby HF activity. The majority of the 191 relocated earthquakes are also temporally correlated with the injection activity at the three HF wells shown in Figure 1b. These three were the only active wells in the region during the study period. The first sequence near the HF well W1 demonstrates a clear pattern of seismicity migration away from the well toward the southeast, similar to the spatiotemporal migration observed at another HF well within 3 km of the MG stations (as shown in Yu *et al.*, 2019) and can be interpreted by pore-pressure diffusion close to the well. We note that our relocated earthquake locations are similar to those from Mahani *et al.* (2017) with an average discrepancy of no more than ~ 2.1 km, which can likely be attributed to the different sets of stations used in the two studies.

We compute the local earthquake magnitudes M_L of the relocated events using the peak *S*-wave amplitude averaged over all stations (see details in the supplemental material), and seismic moment M_0 by fitting the long-period spectral amplitude with a Brune spectral model (details in the single-spectrum fitting section). Figure 2 shows the cumulative seismic moment and daily seismicity rate based on the 191 relocated events and their temporal correlation with the cumulative injection volume during the injection periods at wells W1, W2, and W3 (Fig. 1b). Figure 2 suggests a complex relationship between the seismicity rate at individual wells with respect to daily and cumulative injection volume. First, the lag time between injection onset and the onset of seismicity differs between wells: there is an ~ 5 -day lag at W1, an ~ 1 -day lag at

W2, and an ~ 1 -day lag at W3. Second, a small peak in daily injection rate, and thus cumulative volume, preceded a spike in seismicity on 2 September 2015 by two days. Closer examination of the location of this seismicity spike cluster (shown with thick outlines in Fig. 1b) shows that it began south of the horizontal terminus of the active W1, in close proximity to the M_w 4.6 mainshock and its aftershock sequence. The cluster location suggests a possible reactivation (further stress perturbation) of the same fault system associated with the mainshock. Third, there is lower seismicity in response to injection at W2 compared with W1 and W3. One plausible explanation is that the total injected volume is less, which is also consistent with the conclusions reached by Mahani *et al.* (2017) and Schultz *et al.* (2018), namely that the cumulative amount of injected fluid may be one of the dominant factors in generating induced seismicity. In this study, we focus more on the relationship between individual wells and the corresponding earthquakes, rather than the seismicity rates viewed in the context of total regional injected volumes from all wells in the region as shown in Mahani *et al.* (2017).

STRESS-DROP ESTIMATES

We first use the long-period spectral amplitude Ω_0 of the single-event displacement spectra to constrain the seismic moment M_0 values and to provide initial estimates of corner frequency f_c assuming a constant quality factor Q . We then refine the initial estimates of the spectral corner frequencies for event pairs with similar waveforms and a high signal-to-noise ratio (SNR) over the frequency band of interest using spectral ratios, which minimizes nonsource-related effects

(e.g., Ide *et al.*, 2003; Harrington *et al.*, 2015). In this section, we detail how estimates of M_0 and f_c are used to calculate the static stress-drop values, as well as the refinement of the f_c estimates and stress-drop value estimates.

M_0 and f_c estimates using single spectra

We start with instrument-response-corrected displacement recordings of earthquakes and calculate the phase (P and S) spectra using time windows of 4 and 2 s for earthquakes with magnitudes of $M > 4$ and $M < 4$, respectively. Time windows start 0.1 s before the phase arrival, and spectral estimates are performed using a multitaper spectral estimation on individual components (Thomson, 1982; Prieto *et al.*, 2007). We use the analytical model proposed by Brune (1970, 1971) to estimate values of Ω_0 and f_c from the power spectrum vector sum of all three components as a function of frequency:

$$\Omega(f) = \sqrt{\Omega_{\text{HHZ}}(f)^2 + \Omega_{\text{HHN}}(f)^2 + \Omega_{\text{HHE}}(f)^2}, \quad (1)$$

in which the analytical expression for equation (1) is given by Brune (1970, 1971) as

$$\Omega(f) = \frac{\Omega_0 e^{-\frac{\pi f t}{Q}}}{\left[1 + \left(\frac{f}{f_c}\right)^\gamma\right]^{\frac{1}{\gamma}}}. \quad (2)$$

The parameter t represents the travel time, f is the spectral frequency, f_c is the corner frequency, n is the high-frequency fall-off rate, γ is a constant that determines the spectral corner shape, and Q is the quality factor. Here, we test three models: (1) $\gamma = 1$, and $Q = 1000$ for both P and S waves (Brune model, 1970, 1971); (2) $\gamma = 2$, and $Q = 1000$ for both P and S waves (the assumption of $\gamma = 2$ effectively corresponds to the model proposed by Boatwright, 1980); and (3) $\gamma = 1$, and Q is a free parameter. All three models allow n to vary as an additional free parameter (to Ω_0 and f_c) between 1 and 4. We then use the MATLAB (see Data and Resources) least-squares curve-fitting algorithm and estimate 95% confidence intervals with the asymptotic normal distribution method using the residuals calculated from “Lsqcurfit.” We also compute noise spectra using the same procedure on background noise waveforms of identical window lengths 5 s directly preceding the P -wave arrival (for cases without P -wave arrivals, we use 12 s directly preceding the S -wave arrival, considering an ~ 50 km epicentral distance). The following criteria dictate bandwidth over which the spectra (and spectral ratios) are fitted: (1) SNR > 2 over a bandwidth of at least 15 Hz (we also retain some of the fits with bandwidth > 10 Hz with stable long-period amplitude estimations) and (2) the fitted f_c value is higher and lower than the first and last three spectral data points. We also manually review all spectral fitting results and remove qualitatively poor fits (e.g., in cases in which the spectrum deviates drastically or erratically from the model

at high frequencies) to ensure that f_c values are well constrained between the fitting band limits. A total of 135 of the original 191 relocated events surpass the previous criteria. Figure S4 shows representative examples of single-spectrum fits for P and S phases, and Figure S5 shows the comparison between the three models. We find that (1) the Q -value does not strongly affect the corner-frequency or low-frequency amplitude estimation, and (2) the Boatwright model provides lower corner-frequency estimates compared with the Brune model (thus leading to a smaller stress-drop estimation; Fig. S5). Huang *et al.* (2017) also find a similar systematic trend of lower corner frequencies when the spectral-ratio method is applied with a Boatwright model. The general trend of lower corner frequencies is consistent with the more pronounced spectral fall-off.

Finally, we calculate the seismic moment using the station-averaged Ω_0 values in the following (Eshelby, 1957):

$$M_0 = \frac{4\pi\rho c^3 R\Omega_0}{U_{\phi\theta}}, \quad (3)$$

in which c is the seismic-wave velocity. We assume a constant 5 km/s velocity versus depth, due to poor depth constraints, based on the average velocity of the layers above the hypocenter of the deepest earthquake according to the velocity model (Fig. S1). R is the hypocentral distance, ρ represents density (for which we select the average crustal value of 2700 kg/m³), and the mean radiation pattern $U_{\phi\theta}$ is assumed to be 0.52 and 0.63 for P and S waves, respectively (Aki and Richards, 2002). The moment uncertainties are estimated using a jackknife uncertainty estimation method following the study of Prieto *et al.* (2007).

Corner-frequency refinement using spectral ratios

Once we have the initial estimates of f_c from the single-spectra fitting, we use a spectral-ratio approach to refine the f_c estimation. The single-event earthquake spectrum contains not only energy related to the earthquake source but also information regarding travel path, instrument response, and site effects. Taking the ratio of two collocated earthquake spectra effectively cancels all nonsource-related terms within the spectra, thereby removing any bias or influence on the spectral corner frequency (e.g., Ide *et al.*, 2003; Viegas *et al.*, 2010; Abercrombie, 2013). We refer readers to Abercrombie *et al.* (2017) for a more detailed description of the spectral-ratio approach. We find suitable collocated event pairs for the spectral-ratio refinement by cross-correlating waveforms within the enhanced catalog, assuming that similar waveforms imply very minor differences in hypocentral locations. We also apply additional criteria detailed later for the event pair selection and refer to the larger magnitude event as the master event and the smaller magnitude event as the empirical Green’s function (eGf).

Potential spectral-ratio pairs must satisfy three criteria: (1) the magnitude difference between the bigger and the smaller events must be at least 0.5 to ensure resolvable f_c values, (2) the (relocated) catalog location distance between events in a pair may not exceed 5 km, and (3) the cross-correlation value must exceed 0.7 for P and S phases within individual event pairs. The latter two criteria will only be fulfilled for approximately collocated events with similar focal mechanisms. We then calculate the master event and eGf spectral estimation using the same time-window length convention as the master event. The eGf spectra are recomputed here due to the fact that the time-window length in the single-spectrum estimation is based solely on the earthquake magnitude and thus may vary slightly.

We calculate spectral ratios for each event pair at all stations that fulfill the previous criteria following the stacked spectral-ratio approach (Huang *et al.*, 2016). Stacking spectral ratios across stations produces better-constrained parameter fits by reducing noise and potential radiation pattern effects relative to fitting individual spectral ratios (Huang *et al.*, 2016; Abercrombie *et al.*, 2017). We then fit the stacked spectral ratios using the analytical expression for the ratio of two Brune spectra (Brune, 1970, 1971):

$$\frac{M_1(f)}{M_2(f)} = \frac{\Omega_{01}}{\Omega_{02}} \left(\frac{1 + (f/f_{c2})^\gamma}{1 + (f/f_{c1})^\gamma} \right)^{\frac{1}{\gamma}}, \quad (4)$$

in which f_{c1} , f_{c2} and Ω_{01} , Ω_{02} are the corner frequencies and long-period spectral amplitude values for the master and eGf events, respectively. The high-frequency fall-off parameters n and γ are set to 2 and 1, respectively (e.g., Viegas *et al.*, 2010; Abercrombie, 2014; Abercrombie *et al.*, 2017; Shearer *et al.*, 2019). We also test the Boatwright model with $\gamma = 2$. The generally higher residuals suggest that the Brune model provides a better fit to our data set. The free parameters (Ω_{01}/Ω_{02} , f_{c1} , and f_{c2}) are fit using a least-squares curve fitting algorithm in MATLAB. Although the high- and low-frequency amplitudes of the ratio are fit, we only retain the estimated f_{c1} , and f_{c2} values for refinement. The long-period amplitude values from the single-spectrum fitting are used for the moment and magnitude estimations as they are less affected by attenuation compared with spectral estimates at higher frequencies (such as the corner frequency).

We retain the refined f_c parameter estimates from the spectral-ratio fits based on several imposed criteria. First, the fitted f_{c1} value (master event) should be at least four data points larger than the low-frequency limit of fitting. Second, we perform a grid search in increments of 0.1 Hz surrounding the best-fit values of f_{c1} and f_{c2} in which the misfit values are calculated for each of the fixed f_c values in the grid search (e.g., Viegas *et al.*, 2010; Abercrombie *et al.*, 2017). We discard event pairs for which the grid-search misfit curve does not have a

parabolic shape, and we require a corner-frequency uncertainty for f_{c1} within a factor of 2 of the f_{c1} measurement ($(f_{c1 \max} - f_{c1 \min})/f_{c1} = f_{c1 \text{err}} \leq 2$) following the study of Abercrombie (2014). Finally, we retain the f_{c1} and f_{c2} estimates with the minimum variance for each event pair, for which the errors are determined from the 95% confidence interval of the misfits calculated via the grid search. An example of a spectral-ratio pair using the M_w 4.6 mainshock is shown in Figure 3, and a representative example of a smaller event pair is shown in Figure S6.

Where a master event can be associated with multiple eGfs, we take the invariance weighted mean of all possible master and eGf event pairs. The inverse-variance weighting method (e.g., Abercrombie, 2014; Abercrombie *et al.*, 2017) calculates the weighted mean of the corner-frequency values estimated from the stacked spectral f_c estimate for each individual event pair using the following two equations:

$$\hat{\gamma} = \frac{\sum_i (\frac{\gamma_i}{\sigma_i^2})}{\sum_i (\frac{1}{\sigma_i^2})}, \quad D^2(\hat{\gamma}) = \frac{1}{\sum_i (\frac{1}{\sigma_i^2})}, \quad (5)$$

in which $\hat{\gamma}$ is the weighted mean of f_c , γ_i is the i th measurement, σ_i is the variance, and D is the standard deviation of the weighted mean. The f_{c2} estimation is often disregarded in the weighted mean corner-frequency calculation because it commonly lies out of the bandwidth with $\text{SNR} > 2$. Other studies have also shown poor resolution and less stability in f_{c2} estimates; thus we only report f_{c1} values in Figure 4 (e.g., Viegas *et al.*, 2010; Abercrombie, 2013). Table S3 lists all of the f_{c1} estimates for cases in which multiple eGfs fulfilled event pair and fitting criteria.

Static stress-drop estimation

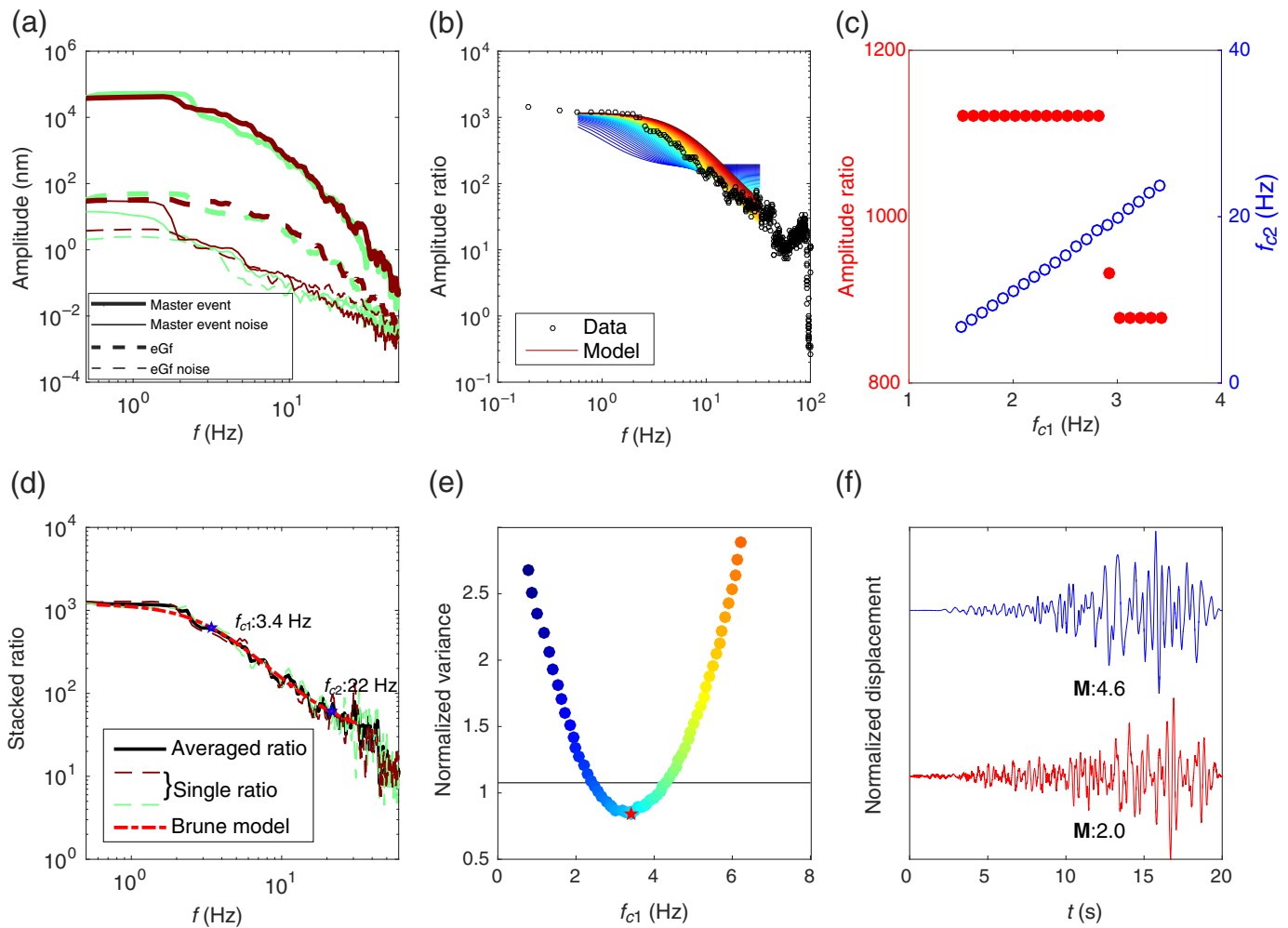
Using values of M_0 and f_c estimated from a single-spectrum fitting and refined f_c values from a spectral-ratio fitting, we calculate the stress-drop values using a circular crack model (Eshelby, 1957):

$$\Delta\sigma = \frac{7}{16} \frac{M_0}{r^3}, \quad (6)$$

$$r = \frac{k\nu}{f_c}, \quad (7)$$

in which $\Delta\sigma$ is the static stress drop, M_0 is the seismic moment, r is the source radius, ν is the phase (P or S) velocity, and k is a constant. Here, we assume values of 5 and 2.8 km/s for the P -wave and S -wave velocities, respectively (due to poor depth constraints), and calculate k using

$$k = \frac{C}{2\pi}, \quad (8)$$



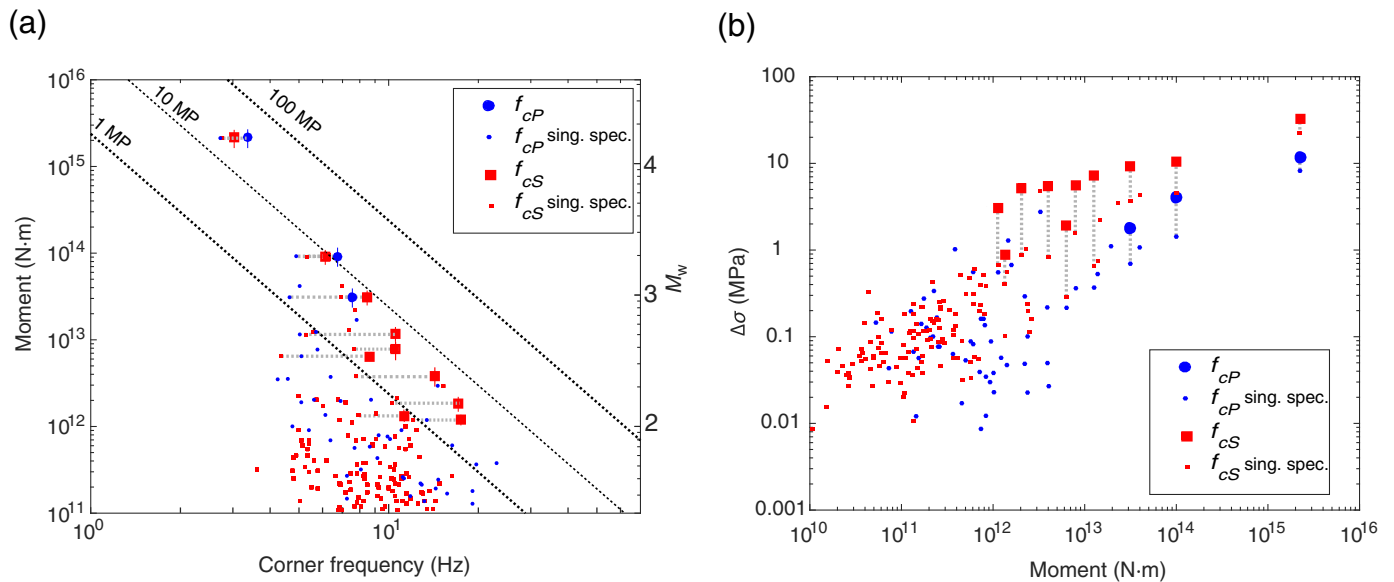
in which C is 1.6 for P waves and 1.99 for S waves, assuming a rupture velocity equal to 90% of the shear-wave velocity (Sato and Hirasawa, 1973). The ratio of P - to S -wave corner frequencies that we estimate from the spectral-ratio method is ~ 0.9 – 1.1 , which is closer to the ratio from the Sato and Hirasawa model of ~ 1.4 , compared with the ratio of ~ 1.5 from the Madariaga model (Madariaga, 1976) (we note that the choice of k is model dependent and should be considered when comparing stress-drop estimates between studies).

Figure 4 shows a comparison of stress-drop values calculated using corner frequencies estimated from both single-spectrum and spectral-ratio fittings based on the Brune model (with $\gamma = 1$). Our result indicates that the corner frequencies estimated from single-spectrum fitting are likely underestimated and that the spectral-ratio estimates more robustly correct for nonsource-related effects, thereby providing better-constrained f_c estimates, as seen in many previous studies (e.g., Ide et al., 2003; Sonley and Abercrombie, 2006; Viegas et al., 2010; Harrington et al., 2015). P -wave stress-drop values range between 1.9 and 15.2 MPa with a median of 6.5 MPa, and S -wave values range between 0.9 and 33.8 MPa with a median of 6.6 MPa.

Figure 3. Representative examples of the spectral-ratio fitting procedure to estimate corner frequency. (a) Vector spectral amplitude (thick line) and noise spectra (thin line) of one master event (solid line) and one empirical Green's function (eGf; dashed line). Each color denotes a spectrum recorded on an individual station. (b) Corresponding data fits for the incremental perturbation of f_{c1} values, with corresponding misfit shown later in (e). Color convention in (b,e) are the same. (c) Corresponding fits of long-period spectral amplitude ratio Ω_1/Ω_2 (solid circles), and f_{c2} between master event and eGf for the f_{c1} increments shown in (b) (empty circles). (d) The best average fit of values f_{c1} and f_{c2} for a Brune spectral model of the stacked spectral ratio. The f_{c1} value is calculated using the weighted mean when multiple secondary events are available (see the [Corner-frequency refinement using spectral ratios](#) section). Same color convention is used as in (a). (e) The misfit of incremented values of f_{c1} , in which each fixed f_{c1} value is represented by a different color. (f) Unfiltered east–west component waveforms recorded at MG04 for both the master event and eGf. The color version of this figure is available only in the electronic edition.

DISCUSSION

Kao et al. (2018) found a lack of a clear pattern between the onset of injection and the delay of seismic activity in north-eastern BC, a feature that makes assessment and management of seismic hazard difficult. One possible explanation for the



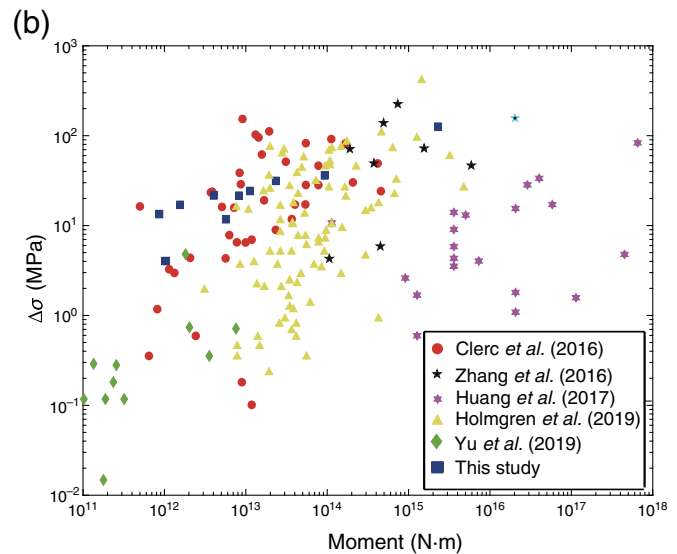
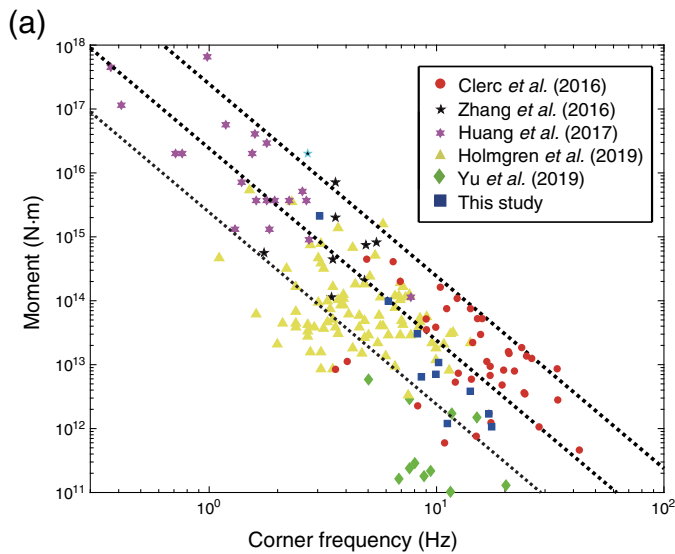
~5-day lag observed at W1 could be that the M_w 4.6 earthquake occurred on a pre-existing fault that was not critically stressed when injection started. The inference of a pre-existing fault is consistent with the b -value of <1 (details in the supplemental material and Fig. S7). The elapsed time allowed a significant amount of injected fluid to reach the fault due to the proximity to W1. The fault-plane solution suggests that the responsible fault was optimally oriented in the regional stress field, which is also consistent with activation of a pre-existing fault. In addition, we note that the maximum magnitude of the induced earthquake at different HF pads could vary considerably, even with a similar injected volume (W1 vs. W3), a scenario also observed in the Sichuan basin, China (Lei *et al.*, 2017). All of the aforementioned characteristics suggest that the seismicity is strongly site dependent and that local geology can play a dominant role. Although we do not observe a clear relationship between the cumulative injected volume and the maximum magnitude of induced seismicity, it is worth noting that, with more fluid injected into the formation, the chance of the injected fluids meeting with a larger fault could also be sufficiently elevated. An extensive discussion of the fault reactivation in the context of the regional stress field, injection history, and injection pressure in the vicinity of the source before, during, and after the rupture nucleation will be presented in a future paper.

If fluids could effectively migrate from the injection point toward the fault, it might suggest the existence of a high-permeability pathway linking the injection points to the pre-existing fault structure, which could lead to accumulated fluid mass and elevated pore pressure that could bring the fault to failure over the ~5-day period. In comparison, the ~1-day lag times at W2 and W3 might be due to the stress perturbations from the continuous pumping at W1 that may have already altered the stress conditions at W2 and W3 through rock

Figure 4. Single-spectrum moment and corner-frequency values and spectral-ratio refined corner-frequency values with corresponding static stress-drop estimations. (a) Big circles and squares indicate corner frequencies for P and S waves estimated using the spectral-ratio approach, respectively. Small circles and squares denote corner frequencies for P and S waves from the single-spectrum fitting, respectively. Black dashed lines mark lines of constant stress drop based on a constant S wavespeed of 2.8 km/s. (b) Stress-drop values versus station-averaged moment values calculated using equation (6). A gray dashed line links estimates from both methods when they are available for the same event. The color version of this figure is available only in the electronic edition.

matrix stress transfer or pore-fluid pressure migration by the time pumping started at the other two wells. In other words, activity at W1 may have brought proximal faults closer to a critically stressed state before pumping at W2 and W3 even began (e.g., Deng *et al.*, 2016; Goebel *et al.*, 2017; Yu *et al.*, 2019) and would be consistent with the relatively shorter observed lag times. It is also important to note that the regional background stress orientation and magnitude, as well as the orientation of the assumed pre-existing fault, will affect the amplitude of the Coulomb stress perturbation (e.g., Lei *et al.*, 2017, 2019). Given the scope of this article, we plan to discuss these factors, including a detailed numerical modeling study, in a future paper.

We calculate the reported cumulative injection volume in proximity to the M_w 4.6 earthquake to check where it stands with respect to the relation between the maximum magnitude and cumulative injection volume proposed in McGarr (2014). The M_w 4.6 event lies above the upper threshold line (see Fig. S8), suggesting that the event magnitude may more likely be controlled by the tectonic setting, as suggested by van der Elst *et al.* (2016). The estimated b -value of 0.78 is also consistent with an interpretation of the tectonic conditions controlling



maximum magnitude (see the supplemental material, and note that the M_w 4.6 earthquake is an outlier of the Gutenberg–Richter [G-R] relationship) and is supported by the interpretation of [Atkinson et al. \(2016\)](#), who suggest that the upper magnitude limit of the HF-induced seismicity could be controlled by the size of the available fault surface. Similarly, as suggested by [Lei et al. \(2019\)](#), the M_w 5.7 induced earthquake sequence in the Sichuan basin, China, not only is an outlier of the G-R scaling relationship but also exhibits a low productivity of the Omori-type aftershocks. They also interpret these features as indicators of induced sequence occurring on a pre-existing fault and that the fault reactivation could be the result of pore overpressure caused by nearby HF operations.

One drawback of using the spectral-ratio method, as opposed to the single-event spectrum fitting to estimate corner frequency is that the number of events for which the method can be applied is relatively low (due to collocation and magnitude difference requirements). Here, we were able to obtain 13 refined corner-frequency estimates using the spectral-ratio method (three for P waves and 10 for S waves, Fig. 4), out of the 191 relocated events in the catalog. The main restricting factor for this study is that most of the eGfs have relatively small magnitudes ($M_w < 1.0$), and have difficulties meeting the SNR requirements. For example, the SNR of the surface stations in this study typically reaches 1 at frequencies of roughly 30–40 Hz, meaning that corner frequencies of earthquakes with $M_w < 2$ become difficult to resolve (e.g., an M_w 2 event with a stress drop of 1–10 MPa would have an estimated $f_c \sim 15$ –30 Hz for S waves).

The smallest master event for which we refine the corner frequency has a magnitude of $M_w \sim 1.9$, meaning that we cannot rule out the possibility that the subtle apparent increase with magnitude of stress-drop estimates shown in Figure 4 could be caused by frequency bandwidth limitations (e.g., [Boatwright, 1994](#); [Viegas et al., 2010](#); [Onwumeka et al., 2018](#)).

Figure 5. (a) Corner frequency versus seismic moment of the induced seismicity in the western Canada sedimentary basin (WCSB) and the central United States (CUS) compiled from different studies. Dashed lines represent lines of constant stress drop assuming a constant shear velocity of 2.8 km/s, the same as shown in Figure 4a,b. Stress-drop values calculated with the Madariaga model for earthquakes as shown in (a). In both plots, circles denote values for the induced earthquakes at Fox Creek, Alberta, from [Clerc et al. \(2016\)](#). Black stars denote the values for induced earthquakes in the WCSB from [Zhang et al. \(2016\)](#); the largest earthquake with light blue outline is a natural earthquake. Triangles denote induced earthquakes in the WCSB from [Holmgren et al. \(2019\)](#). Diamonds denote the induced earthquakes with moment $> 10^{11}$ N · m in the Montney basin from [Yu et al. \(2019\)](#). Hexagons represent the induced earthquakes resulting from wastewater injection in the CUS from [Huang et al. \(2017\)](#). Blue squares denote the stress-drop values derived in this study. The color version of this figure is available only in the electronic edition.

If our maximum resolvable frequency is ~ 30 –40 Hz, it implies we may underestimate corner-frequency values above approximately 13 Hz, which corresponds to the expected corner frequency of an M_w 2.3 event with a 5 MPa stress drop (assuming the S -wave velocity values used here; [Abercrombie, 2015](#), [Abercrombie et al., 2017](#)). In addition, uncertainty becomes larger for parameter estimates of events with moment values below $\sim 10^{13}$ N · m ($M_w \sim 2.3$), partly due to there being fewer eGfs and stations used in the estimates (Table S3). For example, [Abercrombie \(2015\)](#) demonstrates that using one station and one eGf can lead to a standard deviation of 0.2–0.6 times the mean, while using five stations (or five eGfs) can decrease it to below 0.2. In addition, we assume a constant shear-wave velocity when we calculate the stress drop, which can lead to artificial depth dependence, particularly for earthquakes occurring in the upper 5 km of the crust (e.g., [Allmann and Shearer, 2007](#)). However, the poor depth constraints make it difficult to investigate the influence on scaling when a constant velocity is assumed. [Holmgren et al. \(2019\)](#) also suggest that

the station azimuthal coverage could act as a potential factor to influence the corner-frequency estimation. We note that the data set used here suffers from a similar limitation. A consequence is that the derived values of corner frequency (and thus stress-drop estimates) probably represent the lower bound. We not only attempt to mitigate the station coverage issue with the combined usage of MG stations and NRCan stations but also note that the scaling of corner frequency between events should largely remain unaffected by the azimuthal coverage.

Although some studies suggest that the stress-drop values of induced earthquakes are lower than their tectonic counterparts (e.g., Goertz-Allman *et al.*, 2011; Hough, 2014), there are also documented cases of induced earthquakes in the WCSB of stress-drop values on the higher end of the observed range (~ 100 MPa) typical of tectonic events (e.g., Clerc *et al.*, 2016; Zhang *et al.*, 2016). It is important to point out that different studies may use different models to describe the relationship between corner frequency and stress drop, and this may make a direct comparison of stress-drop values between studies difficult. Therefore, we first compare our estimated corner-frequency values with other studies in the WCSB and the CUS in Figure 5a. The result shows that the corner-frequency values fall within the range obtained for other induced events in the WCSB and the CUS, as well as the range commonly observed for tectonic earthquakes.

A similar comparison of the stress-drop values (scaled to a common Madariaga model, as it is commonly used for studies in Canada) shows that, in spite of a possible depth dependence, the values observed in this study are within the middle upper range observed in Clerc *et al.* (2016), Zhang *et al.* (2016), and Holmgren *et al.* (2019) (Fig. 5b). The stress-drop values estimated with spectral ratios do not show significant scaling with event magnitude (values fall within the 1–10 MPa range), indicating that stress-drop values for induced earthquakes may exhibit self-similar behavior, similar to their tectonic counterparts (e.g., Abercrombie, 1995; Goertz-Allman *et al.*, 2011; Harrington *et al.*, 2015; Clerc *et al.*, 2016). Furthermore, they fall within the typical range of induced earthquakes resulting from wastewater injection in the CUS, implying that both wastewater disposal and HF-induced earthquakes may be controlled by tectonic setting once a sequence is initiated (Huang *et al.*, 2017). In terms of seismic hazard assessment, our findings may imply that the same ground-motion prediction equations developed for tectonic earthquakes can be used in areas of induced seismicity.

CONCLUSIONS

We detect more than 300 earthquakes between 11 August and 7 October 2015 related to the 17 August 2015 M_w 4.6 HF-induced earthquake sequence near FSJ, BC, using an enhanced detection method. We relocate 191 earthquakes (Fig. 1b), which exceed the number of NRCan cataloged earthquakes by a factor of ~ 10 for the same time period. Estimated stress-drop

values of ~ 1 –35 MPa are within the range of stress-drop estimates of other HF-induced earthquakes in the WCSB. The delayed seismic response to injection at well W1 supports the statement by Kao *et al.* (2018) that the lack of a clear pattern between injection onset and seismic response makes seismic hazard assessment difficult based on operational parameters alone. A combination of observations, including the range of estimated stress-drop values between ~ 1 and 35 MPa, an observed b -value of 0.78, and a maximum magnitude that is larger than that predicted by injection volume, suggests that the M_w 4.6 occurred on a pre-existing fault (or fault system) and thus is governed by the same statistics used to quantify earthquake behavior on tectonic faults. Therefore, to reduce the potential risks of large HF-induced earthquakes, proximity of HF wells to pre-existing fault structures should be considered in seismic hazard estimation, and the influence of injection may enable reactivation of a fault network beyond the perceived reach of the well.

DATA AND RESOURCES

Earthquake catalog data were obtained from the Natural Resources Canada (NRCan) website available at <http://www.earthquakescanada.nrcan.gc.ca/stndon/NEDB-BNDS/bulletin-en.php>. Seismic waveforms for NRCan stations are publicly available on the Incorporated Research Institutions for Seismology (IRIS) website (network code CN) available at <http://ds.iris.edu/ds/nodes/dmc/forms/breqfast-request/>. Waveform data from MG stations is currently under embargo for a temporary period. MG station data will be available following the embargo, and users who require immediate access may send requests to R. M. Harrington or Y. Liu. Information on unconventional hydrocarbon resources in Canada can be found at <http://www.nrcan.gc.ca/energy/sources/shale-tight-resources/17669>. The supplemental material to this article includes a text document (detailing Global Positioning System [GPS] correction, iterative grid-search location method, and the M_L and b -value calculation), eight figures (velocity model, P - and S -wave phase picking, earthquake initial locations, single-spectrum fitting, source parameter variations based on model fitting, spectral-ratio fitting, b -value and estimation of the magnitude of completeness, and relationship between injected volume and maximum magnitude). In addition, three tables (hypoDD parameters, relocation catalog information, and corner-frequency estimates for master events with multiple empirical Green's functions [eGfs]) are provided. The MATLAB is available at www.mathworks.com/products/matlab. All websites were last accessed in May 2020.

ACKNOWLEDGMENTS

The authors thank two anonymous reviewers for the constructive suggestions. The authors thank Canadian Hazard Information Service and the Induced Seismicity Research Project, Environmental Geoscience Program of Natural Resources Canada (NRCan) for routine maintenance of stations in northeast British Columbia (BC) and Incorporated Research Institutions for Seismology (IRIS) Data Management Center (DMC) for providing data service. The authors would also like to thank Conan Drummond for help with station installation, Mark Norton for station permitting, and Ge Li for providing the travel-path calculation

script. This study is funded by two Natural Science and Engineering Research Council Discovery grants to Harrington and Liu at McGill University, startup funds from the Ruhr University Bochum, and a Geoscience BC grant to Kao. This is NRCan Contribution 20200033.

REFERENCES

- Abercrombie, R. E. (1995). Earthquake source scaling relationships from -1 to $5 M_L$ using seismograms recorded at 2.5-km depth, *J. Geophys. Res.* **100**, 24,015–24,036.
- Abercrombie, R. E. (2013). Comparison of direct and coda wave stress drop measurements for the Wells, Nevada, earthquake sequence, *J. Geophys. Res.* **118**, 1458–1470.
- Abercrombie, R. E. (2014). Stress drops of repeating earthquakes on the San Andreas fault at Parkfield, *Geophys. Res. Lett.* **41**, 8784–8791.
- Abercrombie, R. E. (2015). Investigating uncertainties in empirical Green's function analysis of earthquake source parameters, *J. Geophys. Res.* **120**, 4263–4277.
- Abercrombie, R. E., P. Poli, and S. Bannister (2017). Earthquake directivity, orientation, and stress drop within the subducting plate at the Hikurangi margin, New Zealand, *J. Geophys. Res.* **122**, 176–188.
- Aki, K., and P. G. Richards (2002). *Quantitative Seismology*, University Science Books, Sausalito, California.
- Allmann, B. P., and P. M. Shearer (2007). Spatial and temporal stress drop variations in small earthquakes near Parkfield, California, *J. Geophys. Res.* **112**, doi: [10.1029/2006JB004395](https://doi.org/10.1029/2006JB004395).
- Atkinson, G. M., D. W. Eaton, H. Ghofrani, D. Walker, B. Cheadle, R. Schultz, R. Shcherbakov, K. Tiampo, J. Gu, R. M. Harrington, et al. (2016). Hydraulic fracturing and seismicity in the Western Canada Sedimentary Basin, *Seismol. Res. Lett.* **87**, 631–647.
- Bao, X., and D. W. Eaton (2016). Fault activation by hydraulic fracturing in western Canada, *Science* **354**, 1406–1409.
- B.C. Oil and Gas Commission (2012). Investigation of observed seismicity in the Horn River basin, Technical Rept.
- Boatwright, J. (1980). A spectral theory for circular seismic sources; simple estimates of source dimension, dynamic stress drop, and radiated seismic energy, *Bull. Seismol. Soc. Am.* **70**, 1–27.
- Boatwright, J. (1994). Regional propagation characteristics and source parameters of earthquakes in northeastern North America, *Bull. Seismol. Soc. Am.* **84**, 1–15.
- Brune, J. N. (1970). Tectonic stress and the spectra of seismic shear waves from earthquakes, *J. Geophys. Res.* **75**, 4997–5009.
- Brune, J. N. (1971). Correction to tectonic stress and the spectra of seismic shear waves from earthquakes, *J. Geophys. Res.* **76**, 5002.
- Clerc, F., R. M. Harrington, Y. Liu, and Y. J. Gu (2016). Stress drop estimates and hypocenter relocations of induced seismicity near Crooked Lake, Alberta, *Geophys. Res. Lett.* **43**, 6942–6951.
- Deng, K., Y. Liu, and R. M. Harrington (2016). Poroelastic stress triggering of the December 2013 Crooked Lake, Alberta, induced seismicity sequence, *Geophys. Res. Lett.* **43**, 8482–8491.
- Ellsworth, W. L. (2013). Injection-induced earthquakes, *Science* **341**, 1225942.
- Eshelby, J. D. (1957). The determination of the elastic field of an ellipsoidal inclusion, and related problems, *Proc. Math. Phys. Sci.* **241**, 376–396.
- Goebel, T., M. Weingarten, X. Chen, J. Haffener, and E. Brodsky (2017). The 2016 Mw 5.1 Fairview, Oklahoma earthquakes: Evidence for long-range poroelastic triggering at >40 km from fluid disposal wells, *Earth Planet. Sci. Lett.* **472**, 50–61.
- Goertz-Allmann, B. P., A. Goertz, and S. Wiemer (2011). Stress drop variations of induced earthquakes at the Basel geothermal site, *Geophys. Res. Lett.* **38**, 9.
- Harrington, R. M., G. Kwiatek, and S. C. Moran (2015). Self-similar rupture implied by scaling properties of volcanic earthquakes occurring during the 2004–2008 eruption of Mount St. Helens, Washington, *J. Geophys. Res.* **120**, 4966–4982.
- Holmgren, J. M., G. M. Atkinson, and H. Ghofrani (2019). Stress drops and directivity of induced earthquakes in the Western Canada Sedimentary Basin, *Bull. Seismol. Soc. Am.* **109**, 1635–1652.
- Hough, S. E. (2014). Shaking from injection-induced earthquakes in the Central and Eastern United States, *Bull. Seismol. Soc. Am.* **104**, 2619–2626.
- Huang, Y., G. C. Beroza, and W. L. Ellsworth (2016). Stress drop estimates of potentially induced earthquakes in the Guy-Greenbrier sequence, *J. Geophys. Res.* **121**, 6597–6607.
- Huang, Y., W. L. Ellsworth, and G. C. Beroza (2017). Stress drops of induced and tectonic earthquakes in the central United States are indistinguishable, *Sci. Adv.* **3**, e1700772.
- Ide, S., G. C. Beroza, S. G. Prejean, and W. L. Ellsworth (2003). Apparent break in earthquake scaling due to path and site effects on deep borehole recordings, *J. Geophys. Res.* **108**, no. B001617, doi: [10.1029/2001JB001617](https://doi.org/10.1029/2001JB001617).
- Kao, H., R. Visser, B. Smith, and S. Venables (2018). Performance assessment of the induced seismicity traffic light protocol for northeastern British Columbia and western Alberta, *The Leading Edge* **37**, 117–126.
- Keranen, K., M. Weingarten, G. Abers, B. Bekins, and S. Ge (2014). Sharp increase in central Oklahoma seismicity since 2008 induced by massive wastewater injection, *Science* **345**, 448–451.
- Laske, G., G. Masters, Z. Ma, and M. Pasyanos (2013). Update on CRUST1.0—A 1-degree global model of Earth's crust, *Geophysics Research Abstracts*, EGU General Assembly, Vienna, Austria, Abstract 2658.
- Lei, X., D. Huang, J. Su, G. Jiang, X. Wang, H. Wang, X. Guo, and H. Fu (2017). Fault reactivation and earthquakes with magnitudes of up to Mw4.7 induced by shale-gas hydraulic fracturing in Sichuan Basin, China, *Sci. Rep.* **7**, 7971.
- Lei, X., Z. Wang, and J. Su (2019). The December 2018 M_L 5.7 and January 2019 M_L 5.3 earthquakes in South Sichuan Basin induced by shale gas hydraulic fracturing, *Seismol. Res. Lett.* **90**, 1099–1110.
- Madariaga, R. (1976). Dynamics of an expanding circular fault, *Bull. Seismol. Soc. Am.* **66**, 639–666.
- Mahani, A. B., R. Schultz, H. Kao, D. Walker, J. Johnson, and C. Salas (2017). Fluid injection and seismic activity in the northern Montney play, British Columbia, Canada, with special reference to the 17 August 2015 M_w 4.6 induced earthquake, *Bull. Seismol. Soc. Am.* **107**, 542–552.
- McGarr, A. (2014). Maximum magnitude earthquakes induced by fluid injection, *J. Geophys. Res.* **119**, 1008–1019.
- Moslow, T. F. (2000). Reservoir architecture of a fine-grained turbidite system: Lower Triassic Montney Formation, Western Canada Sedimentary Basin, in P. Weimer, R. M. Slatt, J. Coleman, N. C. Rosen, H. Nelson, A. H. Bouma, M. J. Styzen, and D. T.

- Lawrence (Editors), *Deep-Water Reservoirs of the World, Conference Proceedings, Gulf Coast SEPM*, 686–713.
- Onwuemeka, J., Y. Liu, and R. M. Harrington (2018). Earthquake stress drop in the Charlevoix seismic zone, Eastern Canada, *Geophys. Res. Lett.* **45**, 12,226–12,235.
- Prieto, G. A., D. Thomson, F. Vernon, P. Shearer, and R. Parker (2007). Confidence intervals for earthquake source parameters, *Geophys. J. Int.* **168**, 1227–1234.
- Sato, T., and T. Hirasawa (1973). Body wave spectra from propagating shear cracks, *J. Phys. Earth* **21**, 415–431.
- Schultz, R., G. Atkinson, D. Eaton, Y. Gu, and H. Kao (2018). Hydraulic fracturing volume is associated with induced earthquake productivity in the Duvernay play, *Science* **359**, 304–308.
- Shearer, P. M., R. E. Abercrombie, D. T. Trugman, and W. Wang (2019). Comparing EGF methods for estimating corner frequency and stress drop from *P* wave spectra, *J. Geophys. Res.* **124**, 3966–3986.
- Skoumal, R. J., M. R. Brudzinski, and B. S. Currie (2015). Earthquakes induced by hydraulic fracturing in Poland Township, Ohio, *Bull. Seismol. Soc. Am.* **105**, 189–197.
- Sonley, E., and R. E. Abercrombie (2013). Effects of methods of attenuation correction on source parameter determination, in *Earthquakes: Radiated Energy and the Physics of Faulting*, R. Abercrombie, A. McGarr, G. Di Toro, and H. Kanamori (Editors), 91–97, doi: [10.1029/170GM11](https://doi.org/10.1029/170GM11).
- Thomson, D. J. (1982). Spectrum estimation and harmonic analysis, *Proc. IEEE* **70**, 1055–1096.
- van der Elst, N. J., M. T. Page, D. A. Weiser, T. H. Goebel, and S. M. Hosseini (2016). Induced earthquake magnitudes are as large as (statistically) expected, *J. Geophys. Res.* **121**, 4575–4590.
- Viegas, G., R. E. Abercrombie, and W.-Y. Kim (2010). The 2002 M5 Au Sable Forks, NY, earthquake sequence: Source scaling relationships and energy budget, *J. Geophys. Res.* **115**, no. B006799, doi: [10.1029/2009JB006799](https://doi.org/10.1029/2009JB006799).
- Waldhauser, F., and W. L. Ellsworth (2000). A double-difference earthquake location algorithm: Method and application to the Northern Hayward Fault, California, *Bull. Seismol. Soc. Am.* **90**, 1353–1368.
- Wang, B., R. M. Harrington, Y. Liu, H. Kao, and H. Yu (2018). Remote dynamic triggering of earthquakes in three unconventional Canadian hydrocarbon regions based on a multiple-station matched-filter approach, *Bull. Seismol. Soc. Am.* **109**, 372–386.
- Wang, B., R. M. Harrington, Y. Liu, H. Yu, A. Carey, and N. J. Elst (2015). Isolated cases of remote dynamic triggering in Canada detected using cataloged earthquakes combined with a matched-filter approach, *Geophys. Res. Lett.* **42**, 5187–5196.
- Weingarten, M., S. Ge, J. W. Godt, B. A. Bekins, and J. L. Rubinstein (2015). High-rate injection is associated with the increase in US mid-continent seismicity, *Science* **348**, 1336–1340.
- Yu, H., R. M. Harrington, Y. Liu, and B. Wang (2019). Induced seismicity driven by fluid diffusion revealed by a near-field hydraulic stimulation monitoring array in the Montney Basin, British Columbia, *J. Geophys. Res.* **124**, 4694–4709.
- Yu, H., Y. Liu, R. M. Harrington, and M. Lamontagne (2016). Seismicity along St. Lawrence Paleorift faults overprinted by a meteorite impact structure in Charlevoix, Québec, Eastern Canada, *Bull. Seismol. Soc. Am.* **106**, 2663–2673.
- Zhang, H., D. W. Eaton, G. Li, Y. Liu, and R. M. Harrington (2016). Discriminating induced seismicity from natural earthquakes using moment tensors and source spectra, *J. Geophys. Res.* **121**, 972–993.

Manuscript received 15 October 2019

Published online 7 July 2020